Simulation of Multicomponent Losses in Electron Beam Melting and Refining at Varying Scan Frequencies*

A. Powell** J. Van Den Avyle B. Damkroger J. Szekely**

12 October 1995

Sandia National Laboratories, Albuquerque, New Mexico
**Massachusetts Institute of Technology, Cambridge, Massachusetts

Abstract

A two-stage model is presented to describe alloy element evaporation rates from molten metal due to transient local heating by an electron beam. The first stage is a simulation of transient phenomena near the melt surface due to periodic heating by a scanning beam, the output of which is the relationship between operating parameters, surface temperature, and evaporation rate. At high scan rates, this can be done using a simple one-dimensional heat transfer model of the surface layer; at lower scan rates, a more complex three-dimensional model with fluid flow and periodic boundary conditions is necessary. The second stage couples this evaporation-surface temperature relationship with a larger steady state heat transfer and fluid flow model of an entire melting hearth or mold, in order to calculate local and total evaporation rates. Predictions are compared with experimental results from Sandia's 310-kW electron beam melting furnace, in which evaporation rates and vapor compositions were studied in pure titanium and Ti-6%Al-4%V alloy. Evaporation rates were estimated from rate of condensation on a substrate held over the hearth, and were characterized as a function of beam power (150 and 225 kW), scan frequency (30, 115 and 450 Hz) and background pressure (10^{-3}, 10^{-4} and 10^{-5} torr).

1 Introduction

The electron beam melting and refining process, shown schematically in figure 1, has a number of features which make it an excellent tool for refining high-purity metals. For example, high local temperatures near the beam impingement zone lead to strong stirring due to a large temperature gradient, to fast dissolution or melting of inclusions, and to fast vaporization of volatile impurities such as Pb, Bi and Cd [1]. The large area of metal surface exposed to high vacuum enhances this vaporization effect.

However, these same features which contribute to the biggest strengths of the process also lead to some of its principal weaknesses. In particular, high local temperatures generated by the beam can evaporate alloying elements at very different rates, thus greatly complicating alloy composition control.

Several experimental studies have characterized the effect of beam scan frequency on evaporation rates [2] [3] [4] [5], but to date there have yet to be any general models incorporating that

*This work performed at Sandia National Laboratories is supported by the U. S. Department of Energy under contract number DE-AC04-94AL85000.

parameter.[1] Here we discuss qualitatively the relationship between scan frequency and evaporative losses. We then present a quantitative model to approximate that relationship at very high frequencies, and modifications to adapt that model for somewhat lower frequencies. Finally, we compare model predictions with the results of two experiments performed at Sandia National Laboratories, which studied the effect of process parameters on evaporation rate of commercially pure titanium and on composition of evaporant from a Ti-Al-V alloy pool.

2 Scan Frequency and Evaporation Modeling

Because evaporation rate is a strong and highly nonlinear function of temperature, it is extremely sensitive to temperature fluctuations. These fluctuations are governed by the beam power, residence time, frequency, and ability of the molten material to dissipate heat from the surface. Evaporation can be said to fall into the following regimes, which are discussed as they are affected by deflection frequency for a given pattern geometry:

1. At very high frequencies, dwell times will be very short and temperature fluctuations very small, so the beam power can be considered to be uniformly distributed over the scan pattern.

2. At high frequencies, the beam will generate surface temperature changes large enough to affect evaporation rates, though they do not cause significant transient fluid flow.

3. At moderate frequencies, transient flow generated by Marangoni shear is strong enough to significantly modify temperature fluctuations and affect evaporation rates.

4. At low frequencies, various other phenomena will affect surface temperatures, such as turbulent fluid flow, ionized metal vapor interfering with the beam [12], and depressions in the melt surface generated by large vapor pressure excursions at high temperatures [13].

The exact transitions among these various regimes are hard to define, and depend on the accuracy to which one desires to know the evaporation rate. That said, a rough transition point between regimes 1 and 2 can be estimated relatively easily using the program presented here for regime 2 calculations; the Peclet number describes the transition to regime 3 and can be estimated analytically; and transitions to regime 4 must be determined by the particular phenomena which complicate the problem, e.g. using the Reynolds number to predict the onset of turbulence.

Regime 4 behavior will often affect fluid flows in the whole hearth, but a model for losses in regime 1, 2 or 3 need only consist of a full hearth model coupled with top surface thermal and mass transfer boundary conditions as follows:

$$\vec{q}\cdot\hat{n} = \sum_{i=1}^{N} \frac{\Delta H_{vi} p_{vi}}{\sqrt{2\pi m_i kT}} + \epsilon\sigma(T^4 - T_0^4) - \Phi(x,y)\left(\frac{P_{\text{net}}}{\int \Phi dA} - \Delta q\right) \tag{1}$$

$$\vec{J}_i\cdot\hat{n} = \frac{p_{vi}}{\sqrt{2\pi m_i kT}} + \Phi(x,y)\Delta J_i \tag{2}$$

where $\vec{q}$ and $\vec{J_i}$ represent flux vectors of heat and solute i (out of total solutes N). Equation 1 includes terms for heat loss due to evaporation (ΔH_{vi} is the combined heat of solution and

[1] Of the many efforts to model the process [6] [7] [8] [9] [10] [11], only those of Nakamura and Mitchell and of Powell *et al.* dealt with the effect of this parameter, and those models were only applicable to a narrow range of problems.

vaporization for solute i) and radiation, heat input from the beam (P_{net} is the beam power less losses to x-rays and secondary/backscattered electrons), and enhanced heat losses Δq in regimes two and three. The right side of equation 2 consists of terms for constant-temperature Langmuir evaporation rate and enhancement ΔJ_i due to fluctuating temperature under the beam in regimes 2 and 3. The function $\Phi(x, y)$ represents the beam power distribution function across the top surface, normalized such that its maximum value is unity.

2.1 Regime 1: Full Hearth Model

Evaporation rates in regime 1 have been studied extensively by Nakamura and Mitchell [6], Ablitzer *et al.* [8] [9] and McLelland *et al.* [10]. With the exception of Nakamura and Mitchell, those models simulated a full hearth by solving the strongly coupled Navier-Stokes and energy transport equations in the melt (with buoyancy), and the heat conduction equation in the skull, along with the temperature and flux continuity boundary condition at the melting front or a continuous mushy region between the melt and skull. On the top surface, the study of McLelland *et al.* stands alone in its application of the free surface fluid boundary condition, but all of these models incorporated Marangoni shear and used a heat flux thermal boundary condition consisting of the difference between net heating due to the beam and losses due to radiation and metal evaporation (i.e. eqs. 1 and 2, $\Delta q = \Delta J_i = 0$).

In the present study we solve the same equations in the skull, melt, top surface and melting front, though we use a melting front of lower dimensionality than the number of free surface nodes to obtain fast convergence. We use the FIDAP software package to model one quarter of the hearth in three dimensions and under conditions which mimic those of our evaporation experiments, and assume symmetry in the longitudinal and lateral directions. Composition is assumed to be roughly uniform and to have negligible effect on heat transfer and fluid flow, so overall evaporation rate from the pool can be determined by calculating local Langmuir evaporation rates from local temperatures, integrating these over the melt surface, and multiplying this result by four since our model only covers one quarter of the hearth. Deposition rate on the substrate used in experiments is calculated by integrating the product of the local evaporation rate and viewfactor to the substrate over the whole hearth surface, that is, with different sets of viewfactors for each of the four quarters of the hearth.

Total power level for these simulations was varied over the range used in our experiments from 150 to 270 kW. Melt and skull properties were taken to be those of pure titanium as given in *Smithells Metals Reference Book* [14], and melting front temperature set to 1667°C for c.p. titanium and 1610°C for Ti-6-4.

Figures 2 and 3 show calculated temperatures and melt velocities on the top surface and symmetry planes for c.p. titanium melted at a total beam power of 150 kW (P_{net} = 115kW). It is clear from figure 3 that Marangoni shear on the top surface and the natural convection boundary layer at the edge of the melt pool are the dominant drivers of fluid flow in the pool, and that in the center of the melt pool, temperatures are more-or-less stratified.

2.2 Regime 2: Conduction in the Surface Layer

When the transient motion of the beam has an effect on the evaporation characteristics, modeling such characteristics would seem at first to require a time-stepped simulation of the beam's travels over the whole hearth, which would be extremely computationally intensive. However, if the beam moves through the pattern relatively quickly, the depth of the layer heated during one complete scan will be much smaller than the width of the beam heat affected area, so as long as the Peclet

number is small (indicating transient thermal convection can be neglected), vertical conduction will dominate the transfer of heat away from the surface.

For this reason, transient temperature fluctuations near the surface can be considered locally one-dimensional, and the increase in losses for a given average surface temperature can be calculated by simply solving the heat conduction equation in one dimension. Unfortunately, the highly nonlinear nature of thermal losses at the surface makes the problem analytically intractable, but it is an easy problem to solve numerically, as has been done here.

The program written to solve this problem simulates transient heat transfer through the top layer of the melt, down to a depth $\delta_T = 4\sqrt{\alpha t}$ where α is the thermal diffusivity and t is the period of beam rastering (the inverse of the frequency). Below this depth, temperature does not change significantly. Time iteration is trapezoidal by default but can be adjusted anywhere from fully explicit to fully implicit, and convergence at each time step typically takes two to four iterations.

On the bottom of this surface layer temperature is held constant. On the top, heat flux is given by the difference between heat input from the beam and losses due to radiation and evaporation. The beam is modeled as the projection onto a point of a traveling Gaussian heat flux, which is thus a Gaussian distribution in time. High voltage simulations, in which the beam penetrates a significant fraction of surface layer thickness, introduce the beam as a volumetric heat source instead of a surface source, in which the penetration depth and heat generation profile are given by functions in S. Schiller's *Electron Beam Technology* [15, pp. 39-40]. Evaporation rate is assumed to follow ideal Langmuir evaporation into a vacuum.

This top surface layer simulation runs through several beam scan cycles until convergence is reached. A typical history for the last cycle of such a simulation is shown in figure 4. The time-averaged evaporative flux for a given species in solution is then calculated from the surface temperature history. (If there is significant transient solute depletion at the surface, such depletion can be calculated by the program and will affect this average flux). Average flux is plotted over a range of average surface temperatures calculated in one of two ways. For evaporation rate calculations from temperature surface maps, surface temperature is simply averaged over the last simulated cycle. For coupled process simulations which linearize temperature distribution near the surface, a tangent line in the temperature-depth curve is drawn at the bottom of the simulated layer, and its intercept with the surface is considered to be the average surface temperature, as can be seen on figure 4.

For the simulations presented here, beam power was set to 150 kW, spot diameter to 2 cm, and overall scan pattern length to 2m. Under these conditions, peak power density is about 24 kW/cm^2, and dwell time is one hundredth the beam scan period. Figures 5 show calculated evaporation-temperature relationships for titanium, with evaporation given in $\frac{mol}{cm^2 \cdot sec}$, at three different frequencies and using the latter definition of average surface temperature. It is worth noting that evaporation rates at 450 Hz are not significantly different from those at constant temperature for titanium, making this frequency the approximate threshold for regime 1 behavior.

Also, enhanced titanium losses at 30 Hz, which are about 40% higher than constant temperature losses near the melting point and 25% higher at a 200°C superheat, are of the same order of magnitude as the 17% increase in titanium evaporation rate measured by Melde *et al.* [4, p. 79] when going from 20 ms to 300 ms dwell time. The higher values predicted by the model are due to the fact that the model deals with losses directly in the path of the beam, while most of the hearth is not in that path and will not exhibit such strong temperature fluctuations. It is also possible that 30 Hz is close to being in regime 3, in which case transient fluid flow lowers the maximum surface temperature and evaporation rate a small amount.

A surprising result of the study is that the model predicts no significant change in the total

radiative and evaporative heat losses from the surface. In fact, losses rise by less than three tenths of a percent even at the relatively low frequency of 30 Hz, as shown in figure 6. Because of this, under the conditions described here the effect of scan frequency on thermal losses can be ignored in larger steady-state simulations of a hearth or mold.

2.3 Regime 3: Periodic 3-D Control Volume

Even more so than regime 2, regime 3 evaporation modeling would seem to require a computationally intensive full hearth transient simulation in which the beam is represented as a Gaussian scanning back and forth across the whole surface. However, two years ago the authors introduced an alternate approach illustrated in terms of welding, in which one can either move the heat source or move the workpiece under a stationary heat source. This approach followed the latter course, representing the beam as a stationary heat source of Gaussian distribution and setting boundary conditions that effectively make the fluid move relative to the beam. Typical temperature and melt velocity fields resulting from this approach are shown in figure 7.

This control volume model works only when we neglect interactions between successive passes of the beam on the melt surface. However, that assumption is typically not valid in regime 3 melting where such interactions have a strong effect on flow driven by surface tension gradients. For this reason, it is proposed that this control volume be expanded using periodic boundary conditions as shown in figure 8, such that a full raster sweep of the beam is modeled as a steady-state simulation. Figure 9 shows a typical calculated top surface temperature profile for the convection-diffusion problem with constant velocity solved under these conditions. This solution was generated by the NEKTON software package, but is not a full solution of the strongly-coupled Navier-Stokes and energy transport equations.

Like the one-dimensional model described above, this model can be used to describe the relationship between average surface temperature and evaporation rate, then this relationship coupled with a full hearth or mold fluid flow and heat transfer simulation to deduce the overall evaporation rate of alloying elements.

This is still not a perfect model, in that the lissidue beam scan pattern of a typical melting furnace (such as that used by Melde *et al.* [4]) is approximated by a raster pattern. But in preserving the steady-state nature of the control volume approach while modeling the flows which characterize a regime 3 situation, this model provides an excellent trade-off between efficiency and accuracy which should make it optimally suited for this regime of melting.

3 Experiments

Two sets of experiments were run in the hearth of Sandia National Laboratories Liquid Metal Processing Laboratory electron beam furnace. These examined the effect of process parameters on evaporation rate of c.p. titanium, as measured by vapor condensation rate a known distance above the melt surface, and on the relationship between melt and vapor chemistry in Ti-Al-V melting.

Figure 1 shows a schematic diagram of Sandia's furnace used in both sets of experiments. A water-cooled probe which was inserted for brief intervals during melting to collect melt and vapor condensate. All attachment and removal of these fixtures was done in a small preparation chamber separate from the main vacuum chamber. For these experiments, the 250 kW gun was used alone at power levels from 150 to 265 kW. Other variables included scan frequency, varied from 30 to 450 Hz; background argon pressure between 10^{-5} and 3×10^{-3} torr; and beam focus size set at "small" and "large" (though attempts to measure the actual spot size were unsuccessful).

In the c.p. Ti experiments, desired beam conditions were scanned onto the hearth and held steady for at least seven minutes in order to achieve steady-state pool geometry and skull heat transfer conditions. The probe with vapor-collecting substrate was then inserted to a known position and orientation in the furnace for approximately sixty seconds, and subsequently withdrawn. Thicknesses of films thus deposited were measured by optical microscopy of sectioned substrates.

In the alloy experiments, composition variation was achieved by starting the beam over a charge of as-received Ti-6%Al-4%V and taking melt and vapor samples periodically as aluminum evaporated preferentially out of the melt. After this, a steady state composition was established by melting scrap and flowing it through the hearth to build an ingot at a constant rate. Vapor samples were taken under various beam and chamber conditions After this, c.p. titanium was slowly added to the hearth in order to take two more vapor and melt samples at low vanadium compositions.

Melt and vapor samples were taken by first running the furnace constantly for at least five minutes, then inserting the water-cooled probe with melt capture bolt. At this point, the beam was shut off and the melt capture bolt immediately plunged into the melt and withdrawn from the furnace. The melt capture bolt with melt sample was then removed and replaced with a vapor condensation substrate, which was inserted to a known position in the furnace. With the substrate thus in place, the beam was turned on for approximately thirty seconds to deposit vapor onto its surface, and then shut off. Electron probe microanalysis was used to determine the composition of melt and vapor samples.

3.1 Experimental Results

Condensation rates are shown in table 1, in order of increasing spot size, decreasing total beam power, increasing chamber pressure and increasing frequency. From inspection of the table, a number of surprising trends emerge. For example, evaporation rate appears to rise with increasing frequency, in contrast to well-established experimental evidence in the opposite direction [3] [4] [5]. A possible explanation for this is the inability of the beam deflection system to accurately track the highest frenquencies.

In addition, the highest condensation rates are measured at the highest chamber pressures, which again runs counter to expectations. A suitable explanation for this might be found in focusing effects of beam-plasma interactions, but this is not entirely clear. Evaporation at the larger spot sizes did follow the expected downward trend.

Melt and vapor compositions were measured as described above, and are summarized in table 2. The "evaporation ratio" ER shown in table 2 is defined (for aluminum) as follows:

$$ER_{\mathrm{Al}} = \frac{\mathrm{wt\%Al_{vapor}/wt\%Ti_{vapor}}}{\mathrm{wt\%Al_{melt}/wt\%Ti_{melt}}} \tag{3}$$

Because aluminum is in relatively dilute solution, this ratio will be equal to the equivalent ratio of mole fractions. And the ratio of mole fractions in the vapor is equal to the ratio of Langmuir evaporation rates, so the evaporation ratio can be rewritten as

$$ER_{\mathrm{Al}} = \frac{p_{v\mathrm{Al}}}{X_{\mathrm{Al}}\sqrt{M_{\mathrm{Al}}}} \frac{X_{\mathrm{Ti}}\sqrt{M_{\mathrm{Ti}}}}{p_{v\mathrm{Ti}}} \tag{4}$$

where X_i represents mole fraction of species i in the melt and M_i its molecular weight. Assuming titanium activity roughly follows Raoult's law, its vapor pressure is the product of the vapor pressure in its pure state and mole fraction in the melt, so we rewrite the evaporation ratio again as

$$ER_{\mathrm{Al}} = \frac{p_{v\mathrm{Al}}}{X_{\mathrm{Al}}\bar{p}_{v\mathrm{Ti}}} \sqrt{\frac{M_{\mathrm{Ti}}}{M_{\mathrm{Al}}}} \tag{5}$$

where $\bar{p}_{vi}$ represents the vapor pressure of pure species i. We then use the definition of the activity coefficient $\gamma_{\mathrm{Al}} = \frac{1}{X_{\mathrm{Al}}} \frac{p_{v\mathrm{Al}}}{\bar{p}_{v\mathrm{Al}}}$ to arrive at

$$ER_{\mathrm{Al}} = \gamma_{\mathrm{Al}} \frac{\bar{p}_{v\mathrm{Al}}}{\bar{p}_{v\mathrm{Ti}}} \sqrt{\frac{M_{\mathrm{Ti}}}{M_{\mathrm{Al}}}} \tag{6}$$

This shows that the evaporation ratio is a material property which should be independent of composition at low solute concentrations.

Measured evaporation ratios fell in the range of 16-21 for aluminum and 0.28 to 0.34 for vanadium over the range of process parameters used in the experiment. The ratio of pure element vapor pressures varies considerably, from just over 800 at the melting point of titanium to around 140 at a 500°C superheat for aluminum, and from 0.16 to 0.37 over the same temperature range for vanadium (solid). If we divide the average evaporation ratio for aluminum of 18 by these pure vapor pressure ratios, this effectively bounds the activity coefficient γ_{Al} between 0.024 and 0.11; the same treatment for vanadium bounds $\gamma_{\mathrm{V,\ solid}}$ between 0.78 and 2.19.

Aluminum evaporation ratios were found to decrease with increasing scan frequency, increasing beam power, increasing background gas pressure, and decreasing Al and V content; Vanadium exhibited the opposite tendencies, presumably because of its lower evaporation rate than that of titanium. From the first two correlations, it would seem that the aluminum evaporation ratio is falling with increasing surface temperature (at higher frequency, the pattern narrowed, resulting in higher surface temperatures), so the decreasing pure vapor pressure ratio dominates the typical rise on the activity coefficient toward unity.

It is interesting that although evaporation ratio is related to chemical parameters that are independent of composition, the strongest variation in evaporation ratios occurred when the composition changed (lines 5 and 6 in table 2). This could indicate that aluminum and vanadium concentrations must be very low in order to be in the Henrian regime.

4 Discussion

It is possible that vapor compositions were affected by the practice of starting condensation experiments with the beam playing on solid metal instead of a steady state melt. If diffusion is important in determining vapor composition, then the surface composition of aluminum and vanadium when the guns start is likely to be different from the composition at steady state. Heat transfer will also be somewhat different through an initially solid hearth than a steady-state skull geometry. It should take a very short time to establish the steady-state surface chemistry, but considerably longer to set up a steady-state molten pool configuration in the hearth. Therefore, experimental conditions which allow composition measurements from a molten pool should be investigated further.

The evaporation rate of alloying elements may be complicated by surface solute depletion due to diffusion limitations in the melt. If this is the case, an evaporation model will have to couple mass transport in the hearth or mold with heat transfer and fluid flow in order to accurately predict evaporation rate and composition change; also, a temperature map of the top surface of the hearth will not provide sufficient information to estimate total evaporation rates and alloy composition changes. This can be addressed analytically, and under the operating conditions considered here, transient solute depletion is not likely to be a problem.

The one variable over which we have the least control and of which we have the poorest measurements is the beam spot size. The approximate diameter of 2 cm used here was arrived upon by causing the beam to impinge on a stainless steel plate for a very short time, and measuring the

size of the mark produced, roughly following the method of Suzuki and Watakabe [16, p. 169]. However, it is not certain that this diameter is the appropriate one for the functional form used here. Influence of the beam spot on evaporation rates will likely be via one of two mechanisms: either it will affect the width of the beam path, which will determine the fraction of the hearth surface covered by the beam; or it will affect the rate of transient temperature rise near the beam.

5 Conclusions

Limiting mechanisms for evaporation have been discussed and classified in a set of four regimes of melting. Mathematical models have long existed for evaporation in the first of these regimes, in which the beam is represented as a constant heat source. Here we have introduced efficient models to describe near-surface behavior in the second and third regimes, and discussed results of the model of regime 2 behavior and its coupling to a full hearth model.

For the second regime, a model describing transient heat transfer and evaporation behavior in the melt surface has been constructed and shown by comparison with published experimental data to be reasonably accurate at predicting variation of pure titanium evaporation rate with beam scan frequency. And a method for modeling the third regime based on a steady state simulation of a raster pattern has been introduced and will be further pursued in the near future.

Evaporation rates of pure titanium and vapor compositions from Ti-Al-V alloy melts were successfully measured. Measured evaporation rates followed trends which were not expected, such as increasing evaporation rate with increasing frequency, and increasing evaporation rate with increasing background pressure. The former can be explained by the nature of the equipment used in the experiments, but the latter remains to be explained in our furnace. Evaporation ratios calculated from melt and vapor compositions followed trends which seemed to indicate increasing aluminum evaporation ratio with increasing surface temperature, and the opposite for vanadium.

Acknowledgements

The authors would like to thank P. Randall Schunk of Sandia National Laboratories and Prof. Andreas Alexandrou of Worcester Polytechnic Institute for assistance in developing the computational models presented here. Adam Powell is supported by a CRFP fellowship from AT&T.

References

[1] Lowe, James H. C., "Electron Beam Cold Hearth Refining in Vallejo," *Proc. Conf. EBM&R State of the Art (1994),* 69-77.

[2] S. Schiller, A. von Ardenne and H. Förster "Evaporation of Alloying Elements in EB-Melting–Possibility of Influence," *Proc. Conf. EBM&R State of the Art (1984),* pp. 49-69.

[3] M. Blum *et al.* "Results of Electron Beam Remelting of Superalloys and Titanium Alloys with a High-Frequency EB-Gun," *Proc. Conf. EBM&R State of the Art (1993),* 102-115.

[4] C. Melde, M. Kramer, A. von Ardenne and M. Neumann "The Super Deflection System – a Tool to Reduce the Evaporation Losses in EB Melting Process," *Proc. Conf. EBM&R State of the Art (1993),* 69-80.

[5] C. Melde, G. Jäsch, E. Mädler, "New Developments for High Power Electron Beam Equipment," *Proc. Conf. EBM&R State of the Art (1994),* 51-63.

[6] H. Nakamura and A. Mitchell "The Effect of Beam Oscillation Rate on Al Evaporation from a Ti–6Al–4V Alloy in the Electron Beam Melting Process," *ISIJ Int'l,* **32**, 5 (1992) 583-592.

[7] W. Shyy *et al.*, "Effect of Turbulent Heat Transfer on Continuous Ingot Solidification," *Trans. AIME* **115** (Jan. 1993), pp. 8-16.

[8] D. Ablitzer *et al.* "Mathematical Modeling of Electron Beam Remelting Process: Application to the Processing of Titanium Alloys," *Proc. Conf. EBM&R State of the Art (1992),* 85-94.

[9] J-P. Bellot, E. Floris, A. Jardy and D. Ablitzer "Numerical simulation of the E.B.C.H.R. Process," *Proc. Conf. EBM&R State of the Art (1993),* 139-152.

[10] K. Westerberg, M. McClelland, B. Finlayson "Numerical Simulation of Material and Energy Flow in an E-Beam Melt Furnace," *Proc. Conf. EBM&R State of the Art (1993),* 153-165.

[11] A. Powell, B. Damkroger, R. Fisher, J. Van Den Avyle and J. Szekely "Numerical Simulation of Beam-Melt Interaction in Electron Beam Melting," Presented at Conf. EBM&R State of the Art (1993), submitted to *Metall. Trans. B* January 1994.

[12] D. Tripp, S. Cockcroft and A. Mitchell "The Effect of Pressure on Power Transfer in Electron Beam Remelting," *Proc. Conf. EBM&R State of the Art (1993),* 127-138.

[13] A. Powell, B. Damkroger, R. Fisher and J. Szekely "The Mechanism of Crater Formation in Electron Beam Processing," Presented at the TMS Annual Meeting, February 22, 1993 in Denver, Colorado.

[14] E. Brandes, ed. *Smithells Metals Reference Book (6th edition).* Boston: Butterworth & Co., 1983.

[15] S. Schiller, U. Heisig, S. Panzer. *Electron Beam Technology.* (English translation) New York: John Wiley & Sons, 1982.

[16] K. Suzuki and S. Watakabe "Temperature Measurement and Bath Stirring during Electron Beam Melting of Ti-6%Al-4%V Alloy," *Proc. Conf. EBM&R State of the Art (1993),* 167-178.

Tables

Table 1: Process parameters and measured condensation rates.

Freq., Hz	Power[2], kW	Pressure, torr	Spot size	Measured condensation rate, μm/sec
30	265	1.2×10^{-5}	S	3.49±0.08
115	260	1.1×10^{-5}	S	3.69±0.18
230	260	8×10^{-6}	S	3.92±0.12
450	265	9×10^{-6}	S	4.55±0.10
30	260	9×10^{-5}	S	2.15±0.10
450	265	9×10^{-5}	S	2.32±0.06
30	262	1.0×10^{-3}	S	3.29±0.07
115	260	1.0×10^{-3}	S	4.23±0.09
450	260	1.0×10^{-3}	S	7.54±0.08
30	260	3.0×10^{-3}	S	7.48±0.09
30	165	1.0×10^{-5}	S	2.11±0.05
115	165	1.0×10^{-5}	S	2.14±0.09
450	160	1.0×10^{-5}	S	2.54±0.03
30	155	1.5×10^{-3}	S	1.59±0.12
450	165	1.2×10^{-3}	S	3.14±0.02
30	260	1.0×10^{-5}	L	2.74±0.07
450	260	1.2×10^{-5}	L	3.39±0.03
30	260	2.0×10^{-3}	L	2.22±0.19

Table 2: Process parameters and measured evaporation ratios.

Freq., Hz	Power[2], kW	Pressure, torr	wt%Al_{melt}	wt%V_{melt}	ER_{Al}	ER_V
115	142	6.5×10^{-5}	6.0	4.0	18.70±0.91	0.336±.056
115	224	2.0×10^{-5}	2.84	4.51	18.88±1.92	0.315±.064
115	216	1.0×10^{-5}	1.57	4.47	16.53±0.45	0.291±.020
115	213	8.0×10^{-6}	1.72	4.82	17.10±0.45	0.334±.028
115	224	7.5×10^{-6}	0.83	2.25	15.73±0.36	0.379±.024
115	224	7.0×10^{-6}	0.61	2.33	13.66±0.76	0.388±.020
30	139	2.1×10^{-5}	3.13	4.35	20.85±0.50	0.293±.039
30	221	3.0×10^{-5}	3.13	4.35	20.28±0.97	0.297±.031
30	180	1.7×10^{-3}	3.13	4.35	19.86±0.91	0.283±.025
450	139	2.5×10^{-5}	3.13	4.35	19.47±0.91	0.303±.030
450	230	3.0×10^{-5}	3.13	4.35	16.60±0.60	0.315±.025
450	139	1.1×10^{-3}	3.13	4.35	17.33±0.85	0.341±.030

[2]In both tables, this represents total power input to the electron gun, not net power.

Figures

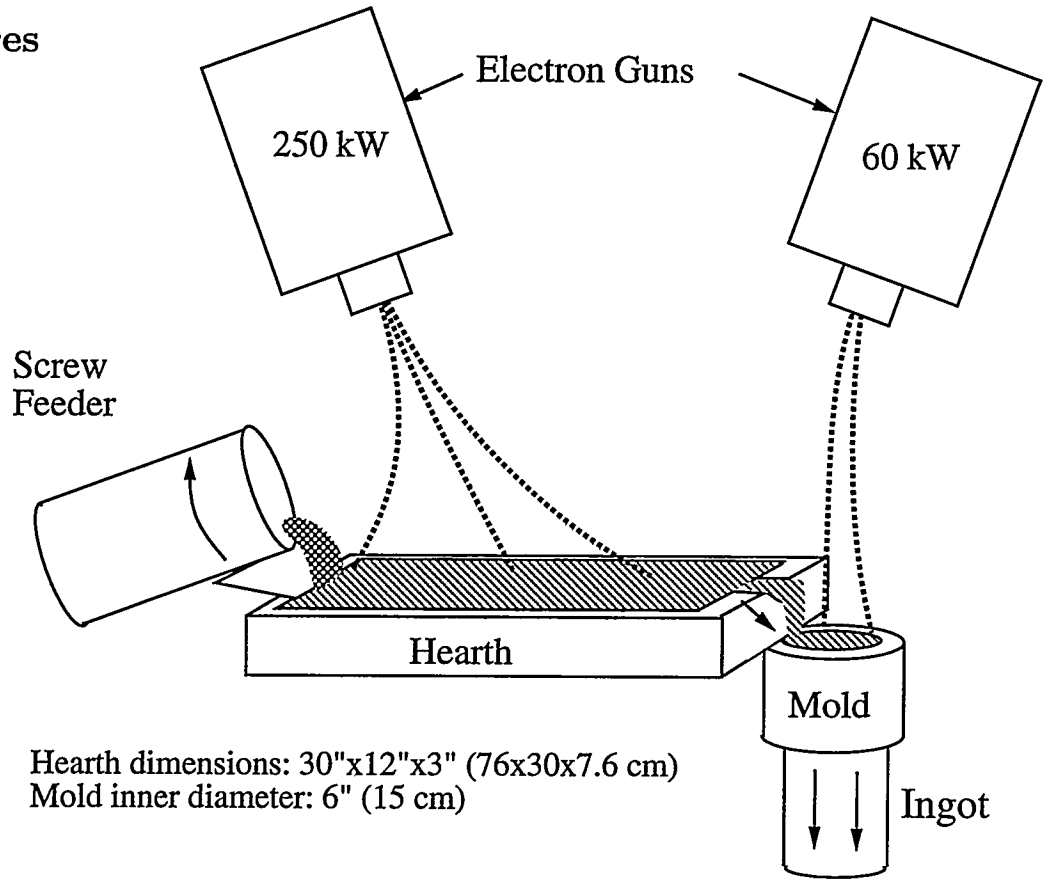

Figure 1: Electron beam melting facility at Sandia National Laboratories.

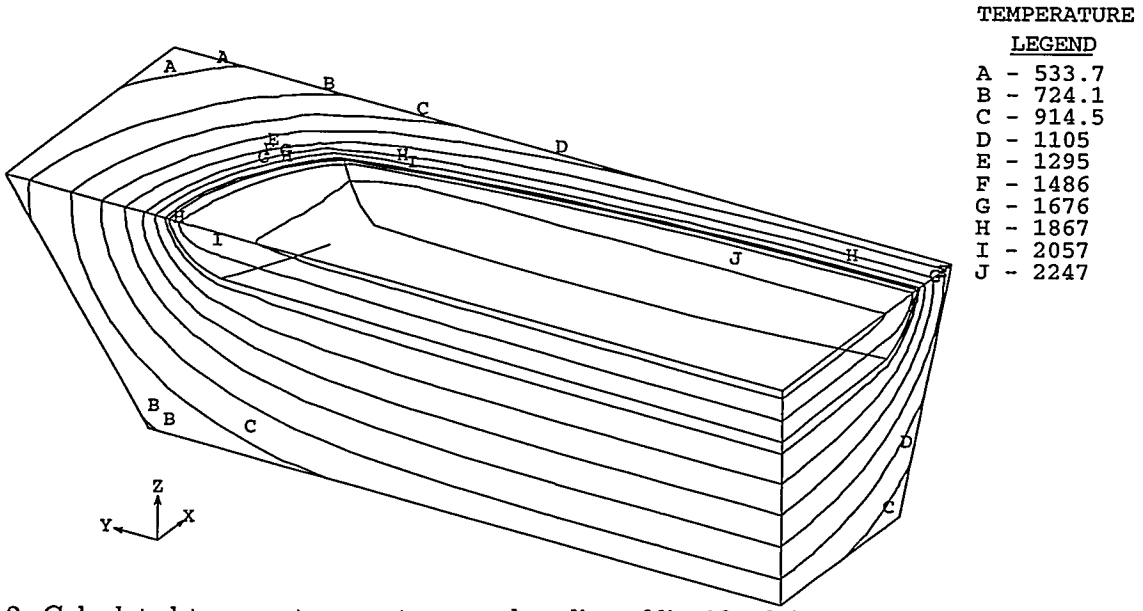

Figure 2: Calculated temperature contours and outline of liquid-solid interface for a 150 kW beam on a hearth 10 cm thick, upper dimensions 75×27 cm, lower dimensions 61×21 cm.

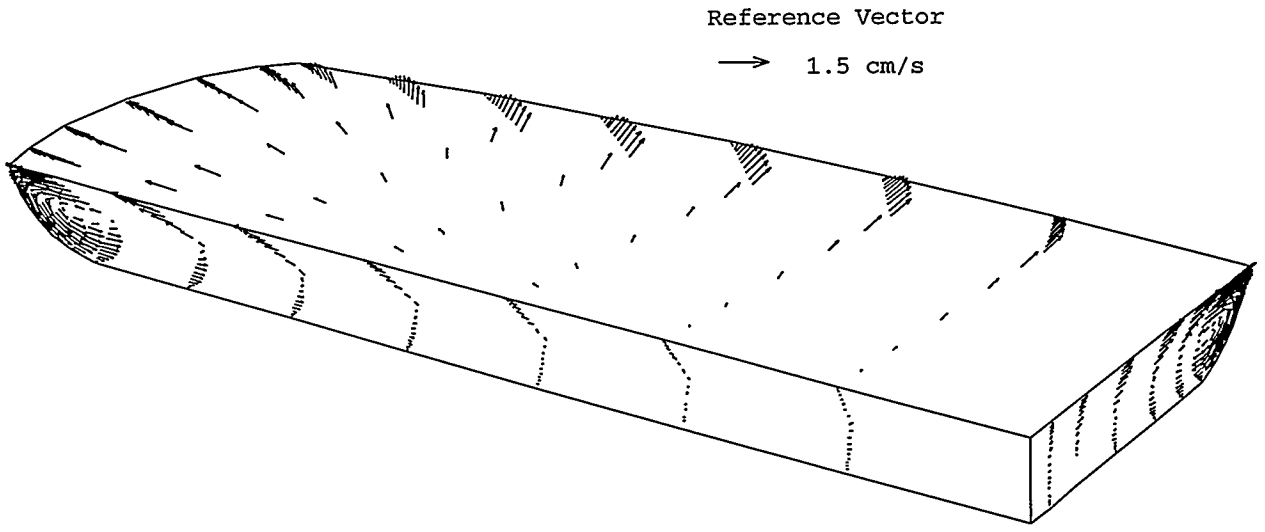

Figure 3: Calculated melt velocity vectors for the simulation presented in figure 2.

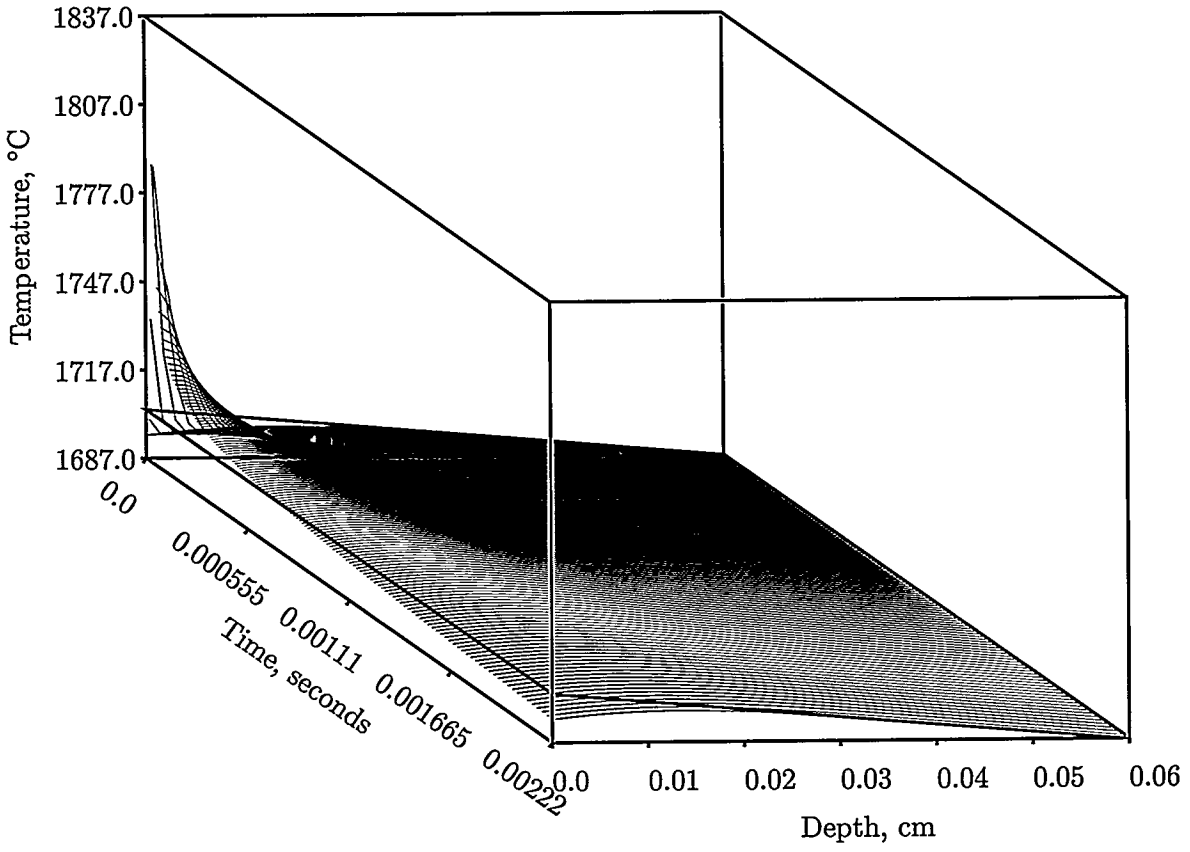

Figure 4: Calculated temperature history in the top surface layer of molten titanium hit by a 150 kW beam for 1/45000 sec at 450 Hz. For clarity, only every other timestep is shown here.

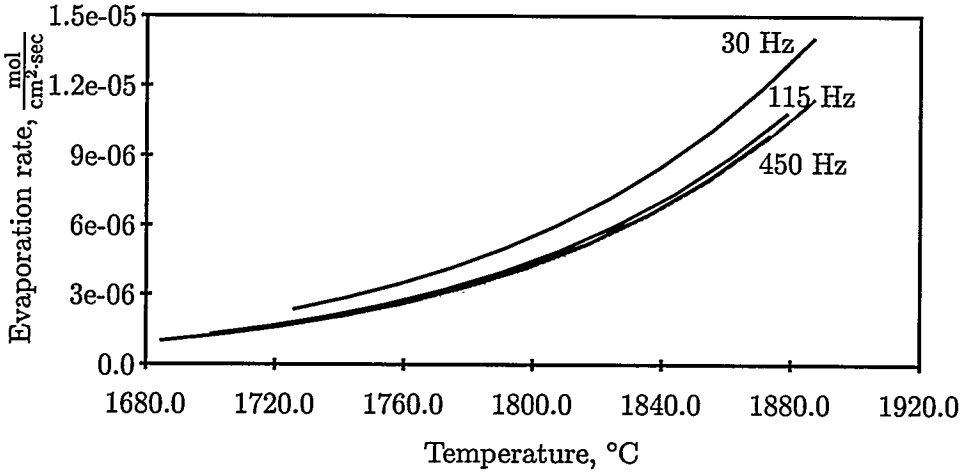

Figure 5: Calculated evaporation rates of pure titanium from a 150 kW (net) beam as a function of average surface temperature at 30, 115 and 450 Hz. The gray curve represents constant temperature evaporation rate.

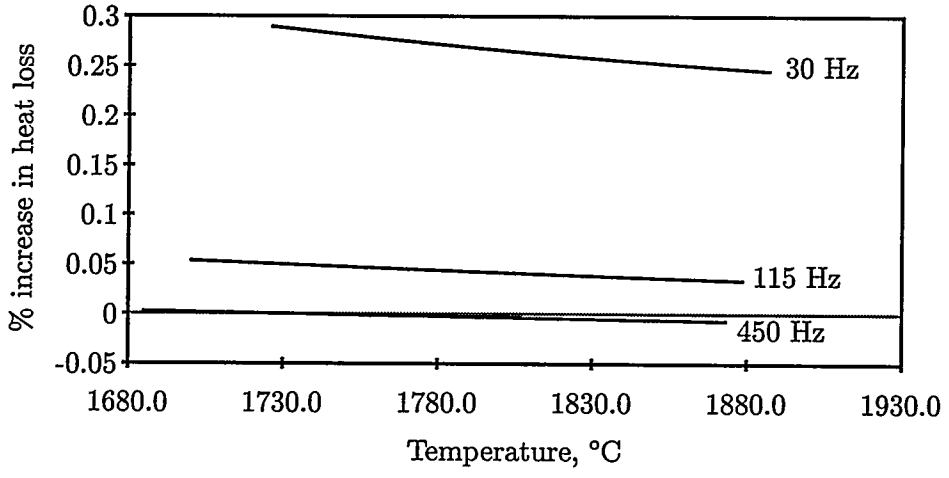

Figure 6: Percentage change of thermal losses vs. constant temperature for a 150 kW (net) beam at 30, 115 and 450 Hz.

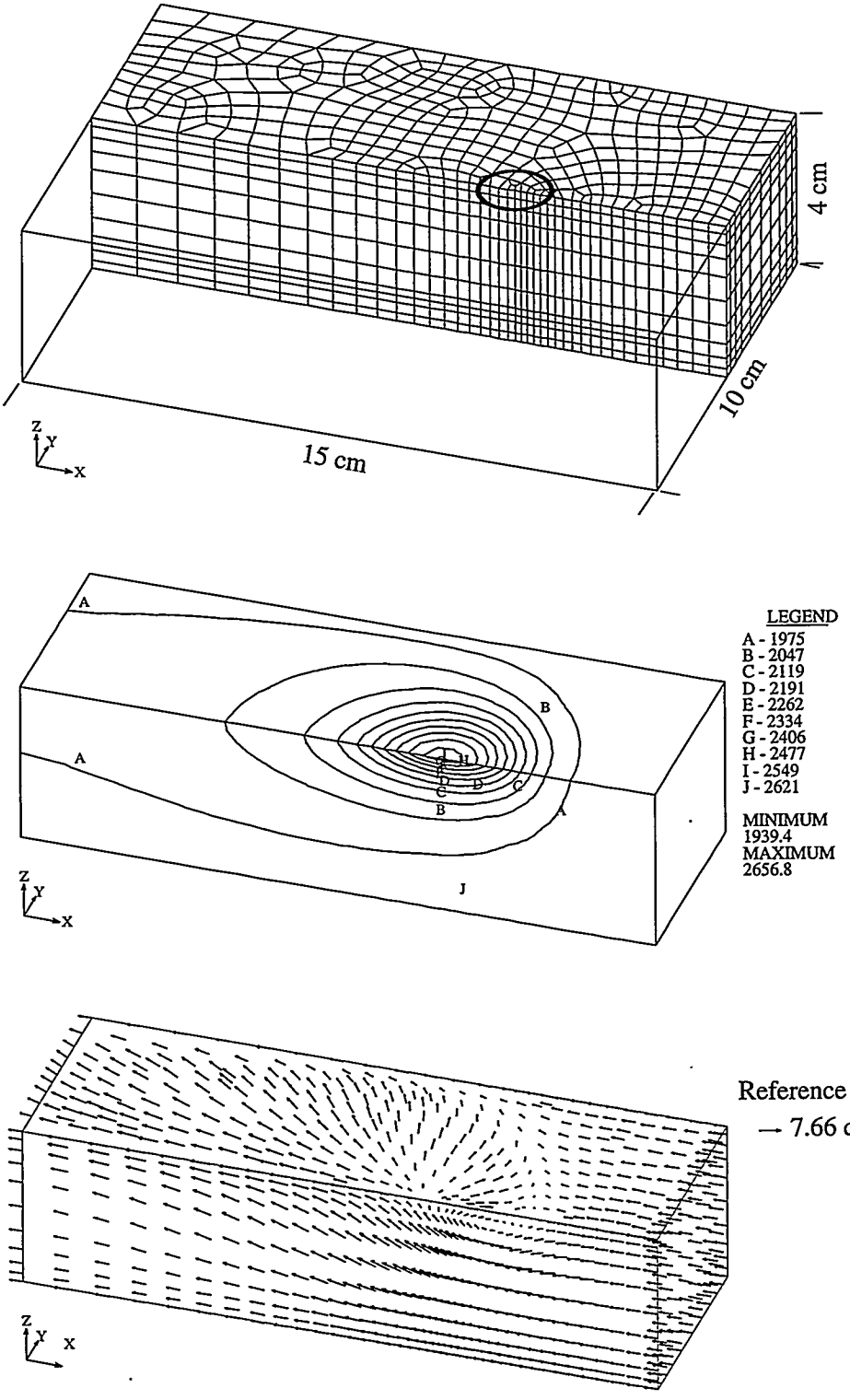

Figure 7: Mesh, temperature and velocity profiles for a "control volume" of molten titanium, and beam location indicated by the black circle.

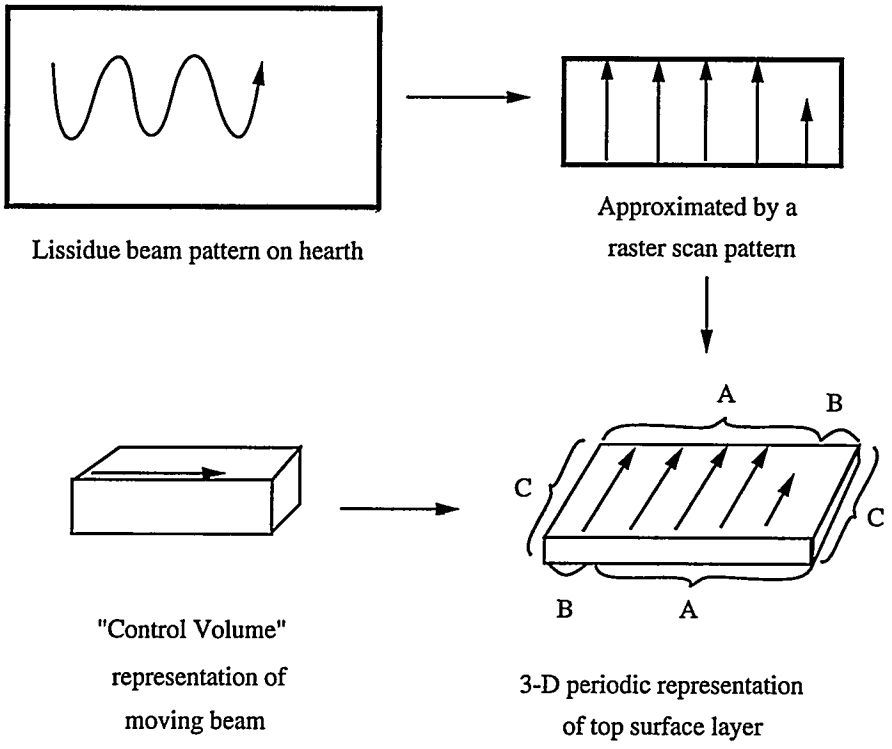

Figure 8: Derivation of the 3-D periodic simulation geometry for regime 3 evaporation modeling.

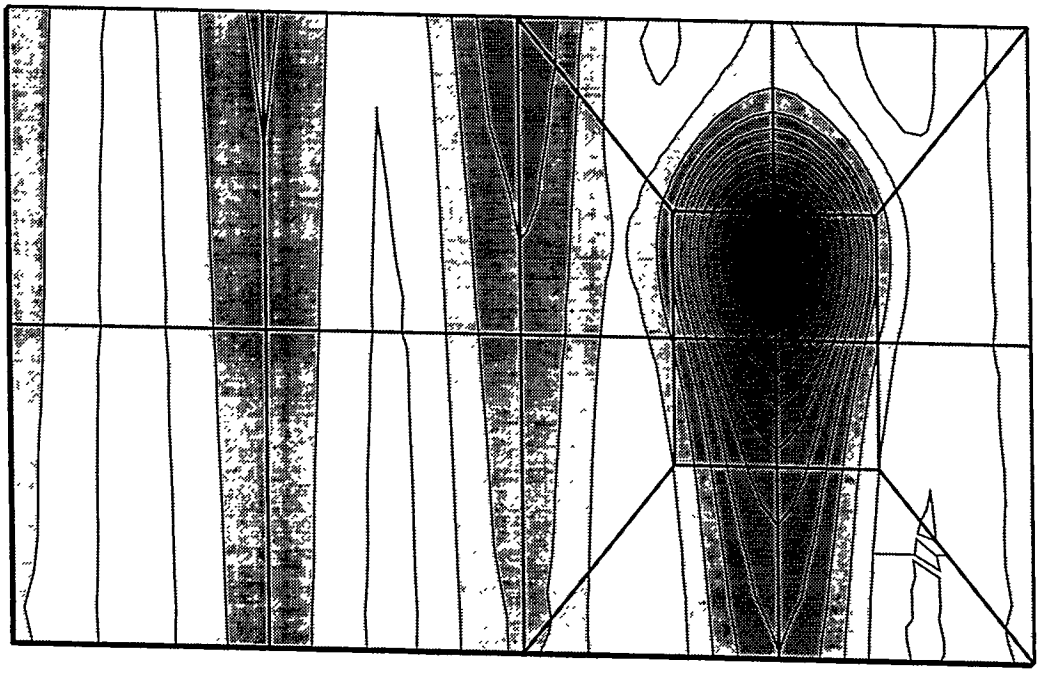

Figure 9: Isotherms of 3-D periodic simulation of top surface layer.

DISCLAIMER